ACS Catalysis

Research Article

pubs.acs.org/acscatalysis

3D Bi_2MoO_6 Nanosheet/TiO_2 Nanobelt Heterostructure: Enhanced Photocatalytic Activities and Photoelectochemistry Performance

Jian Tian,[†,‡] Pin Hao,[‡] Na Wei,[†] Hongzhi Cui,*[,†] and Hong Liu*[,‡]

[†]School of Materials Science and Engineering, Shandong University of Science and Technology, Qingdao 266590, China

[‡]State Key Laboratory of Crystal Materials, Shandong University, Jinan 250100, China

Supporting Information

ABSTRACT: We employed TiO_2 nanobelts as the synthetic template and developed three-dimensional (3D) porous Bi_2MoO_6 nanosheet/TiO_2 nanobelt heterostructures with a few-layer and uniform Bi_2MoO_6 nanosheets by a simple hydrothermal method. The as-prepared Bi_2MoO_6 nanosheet/TiO_2 nanobelt heterostructure shows an excellent photodegradation performance under UV and visible light irradiation. Importantly, such a heterostructure possesses high photocatalytic oxygen production with a rate of 0.668 mmol h^{-1} g^{-1}. Moreover, the Bi_2MoO_6 nanosheet/TiO_2 nanobelt heterostructure shows an enhanced photoelectochemistry performance under irradiation of solar illumination. The current research can offer an alternative route for designing a 3D heterostructure system to effectively utilize broad-spectrum solar light.

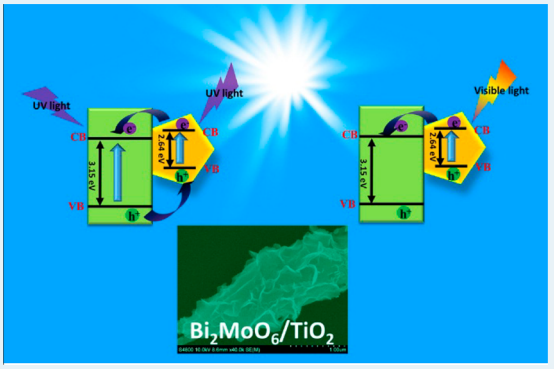

KEYWORDS: *TiO_2 nanobelt, heterostructure, photocatalytic, photoelectrochemistry, oxygen production*

1. INTRODUCTION

In recent years, two-dimensional (2D) flakes decorated on one-dimensional (1D) semiconductor nanostructures to form three-dimensional (3D) heterostructures with versatile properties have been effectively fabricated and highly regarded in various applications, including batteries, photodetectors, and photocatalysis.[1−5] Among these 1D semiconductor nanostructures, TiO_2 has attracted great attention in the production of H_2 or O_2 and the decomposition of pollutants.[6−8] Unfortunately, TiO_2 possesses a wide band gap of 3.2 eV and can be photoactivated under UV light, which accounts for only 4% of the solar energy, thus greatly limiting its practical applications.[9−11] To further utilize visible light, which accounts for the main part (48%) of the incoming solar energy,[12] numerous methods have been made to improve the photocatalytic activity of TiO_2-based photocatalysts, such as metallic or nonmetallic element-doping,[13] and hydrogenation or reduction of TiO_2 to enhance the light absorption.[14] In addition, coupling TiO_2 with an excellent visible semiconductor photocatalyst to form the heterostructure, such as Ag_2O/TiO_2, NiO/TiO_2, and CeO_2/TiO_2,[15−17] has become an efficient approach for improving the photocatalytic property of TiO_2 because the heterostructure can not only broaden the spectral response range to visible light but also promote the charge separation.[18,19]

Bi-based semiconductor materials, such as Bi_2O_3, $Bi_4Ti_3O_{12}$, Bi_2WO_6, and Bi_2MoO_6, as novel kinds of photocatalysts have attracted much attention because of their layer structures and high catalytic properties.[20−22] In particular, Bi_2MoO_6 (E_g = 2.6 eV), as a typical aurivillius oxide and an n-type semiconductor, is a promising visible-light-driven photocatalyst.[23] Recently, Shimodaira et al.[23] found that Bi_2MoO_6 presented excellent photocatalytic oxygen evolution activity under visible light. Bi's group[24] revealed that Bi_2MoO_6 had a high photodegradation property. Subsequently, Guo and co-workers[25] prepared Bi_2MoO_6 nanoplates via a simple solvothermal method and investigated their visible photocatalytic performance. These works revealed that Bi_2MoO_6 could perform as an excellent photocatalyst.

1D nanostructures, such as TiO_2 nanobelts, have aroused great interest because of their high surface areas, chemical stability, and remarkable carrier transport property; thus, their photocatalytic activities are enhanced.[4] 2D semiconductor nanomaterials, such as Bi_2MoO_6 nanosheets, are also of great worth because of their unique layered structures and excellent photocatalytic properties, which can be attributed to their narrow band gap and high surface areas.[25] Therefore, it is believed that 2D Bi_2MoO_6 nanosheets decorated on 1D TiO_2 nanobelts to form 3D heterostructure will be a photocatalyst with superior performance by efficiently utilizing the integrated merits of TiO_2 and Bi_2MoO_6. Moreover, the 3D heterostructure presents a special morphology with high surface areas to capture more light and minimize the transfer distance of charge, improve the separation of photogenerated carriers, and exhibit an improved photocatalytic efficiency.

In this paper, we fabricated 3D porous Bi_2MoO_6 nanosheet/TiO_2 nanobelt heterostructures by using TiO_2 nanobelts as 1D

Received: March 16, 2015
Revised: May 24, 2015
Published: June 4, 2015

DOI: 10.1021/acscatal.5b00560
ACS Catal. 2015, 5, 4530−4536

nanoscale substrates through a hydrothermal method. The coarsened surface of the acid corrosion TiO_2 nanobelts provided numerous growth sites so that the uniform Bi_2MoO_6 layers on TiO_2 nanobelts could be obtained. The photocatalytic activity of the 3D porous Bi_2MoO_6 nanosheet/TiO_2 nanobelt heterostructures was studied for the photodecomposition of methylene orange and photocatalytic oxygen production. In addition, the photoelectochemistry (PEC) performance and the photocatalytic mechanism of the Bi_2MoO_6 nanosheet/TiO_2 nanobelt heterostructures were also discussed.

2. EXPERIMENTAL SECTION

2.1. Materials. Titania P25 (TiO_2), sodium hydroxide (NaOH), hydrochloric acid (HCl), sulfuric acid (H_2SO_4), ethylene glycol, bismuth nitrate pentahydrate ($Bi(NO_3)_3 \cdot 5H_2O$), sodium molybdate dihydrate ($Na_2MoO_4 \cdot 2H_2O$), and ethanol were purchased from Sinopharm.

2.2. Preparation of TiO_2 Nanobelts. P25 (0.2 g) was immersed in 40 mL of a 10 M NaOH solution. The suspension was transferred to a 50 mL Teflon-lined autoclave and maintained at 180 °C for 48 h. After washing thoroughly with deionized water, the obtained products were dissolved in a 0.1 M HCl solution for 48 h to obtain $H_2Ti_3O_7$ nanobelts, then the above products were immersed in a 0.02 M H_2SO_4 solution and maintained at 180 °C for 10 h. After washing thoroughly with deionized water, the sample was annealed at 600 °C for 2 h.

2.3. Preparation of 3D Bi_2MoO_6 Nanosheet/TiO_2 Nanobelt Heterostructure. Bi_2MoO_6 nanosheet/TiO_2 nanobelt heterostructures (mole ratios from 1:1 to 4:1) were synthesized by a coprecipitation hydrothermal method. $Bi(NO_3)_3 \cdot 5H_2O$ (0.4−1.6 mmol), $Na_2MoO_4 \cdot 2H_2O$ (0.2−0.8 mmol), and TiO_2 nanobelts (0.2 mmol) were immersed in 15 mL of ethylene glycol, respectively, and then were mixed together. The resulting suspension was maintained at 160 °C for 24 h in a 50 mL Teflon-lined autoclave. Finally, the products were washed thoroughly with deionized water. For comparison, pure Bi_2MoO_6 nanosheets were also synthesized in the same manner without the addition of TiO_2 nanobelts.

2.4. Characterizations. X-ray powder diffraction (XRD) measurements of catalysts were conducted on a Bruke D8 Advance X-ray diffractometer using Cu Kα (λ = 0.15406 nm) radiation. Scanning electron microscopy (SEM) was performed with a HITACHI S-4800 instrument with an energy-dispersive X-ray spectroscopy (EDS). Transmission electron microscopy (TEM) was carried out with a JEOL JEM 2100F field emission transmission electron microscope. Fourier transform infrared (FTIR) spectra were recorded on a Thermo Nicolet Avatar 370 FTIR spectrometer in KBr pellets. The UV−vis diffuse reflectance spectra (DRS) were tested with a spectrophotometer (UV-2550, Shimadzu). The photoluminescence (PL) spectra were measured with a Raman spectroscope (HR 800, JY) under a laser excitation of 325 nm.

2.5. Photocatalytic Activity Test. The photocatalytic activity of the Bi_2MoO_6 nanosheet/TiO_2 nanobelt heterostructures was examined toward photodegradation of MO and photocatalytic oxygen evolution. In a photodegradation experiment, 20 mg samples were added to 20 mL of aqueous MO solutions in an XPA-photochemical reactor (Xujiang Electromechanical Plant, Nanjing, China). A 350 W mercury lamp was used as the UV light resource. A 300 W Xe arc lamp with filter UV light glasses was used as the visible light source. In a photocatalytic oxygen evolution experiment, catalyst (0.3 g) was added into 100 mL of a 0.05 mol/L $AgNO_3$ aqueous solution. The reaction temperature was maintained at 5 °C. A 300 W Xe arc lamp (CEL-HXF300) was used as the light source. The amount of O_2 evolved was determined with a gas chromatograph (Techcomp GC7900).

2.6. Photoelectrochemical Measurements. Photocurrent density was measured in a three-electrode electrochemical cell in the 0.1 M Na_2SO_4 electrolyte, in which Pt foil and a Ag/AgCl electrode were used as the counter and reference electrodes, respectively. The photocatalysts slurries were deposited on a FTO glass surface and annealed at 400 °C to obtain the working electrode. The $I-t$ curves were measured under solar illumination irradiation (AM 1.5G, 100 mW/cm^2) with light on−off switches of 50 s.

3. RESULTS AND DISCUSSION

3.1. Structure, Composition, and Morphology. The XRD patterns of TiO_2 nanobelts, Bi_2MoO_6 nanosheets, and Bi_2MoO_6 nanosheet/TiO_2 nanobelt heterostructures are shown in Figure 1. For TiO_2 nanobelts (curve a), six distinctive peaks

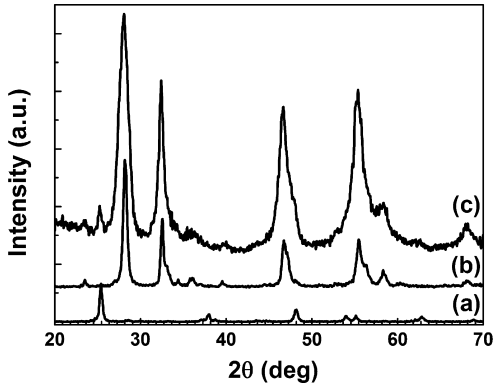

Figure 1. Typical XRD patterns of (a) TiO_2 nanobelts, (b) Bi_2MoO_6 nanosheets, and (c) Bi_2MoO_6 nanosheet/TiO_2 nanobelt (mole ratio 2:1) heterostructures.

at 2θ = 25.28°, 37.80°, 48.05°, 53.89°, 55.06°, and 62.69° match well with anatase TiO_2 (JCPDS 21-1272).[17] In curve b, the diffraction peaks at 28.25°, 32.59°, 33.07°, 46.72°, 47.07°, 55.46°, 55.53°, and 56.16° are observed. These peaks could be perfectly indexed to the (131), (002), (060), (202), (260), (331), (133), and (191) planes of orthorhombic Bi_2MoO_6 (JCPDS 76-2388).[23] For Bi_2MoO_6 nanosheet/TiO_2 nanobelt heterostructures (curve c), all the peaks can be assigned to TiO_2 or Bi_2MoO_6, and no extra peaks are found.

The top inset of Figure 2a presents SEM image of the TiO_2 nanobelts, which are 100−300 nm in width, 30−50 nm in thickness, and tens of micrometers in length.[26] After an acid etching process, surface-coarsened TiO_2 nanobelts are obtained (Figure 2a). They exhibit a high specific surface area and provide abundant nucleation sites for the assembling of Bi_2MoO_6 nanosheets. The Bi_2MoO_6 nanosheets (Figure 2b) synthesized by the hydrothermal method self-assemble to form Bi_2MoO_6 microspheres. These spheres are 2−3 μm in diameter. As shown in Figure 2c and d, the surface of the TiO_2 nanobelts is homogeneously covered with a layer of dense Bi_2MoO_6 ultrathin nanosheets (mole ratio 2:1). Thus, 3D networks are formed, which have a highly porous surface morphology and can act as a fast carrier transfer channel. Moreover, Bi_2MoO_6

DOI: 10.1021/acscatal.5b00560
ACS Catal. 2015, 5, 4530−4536

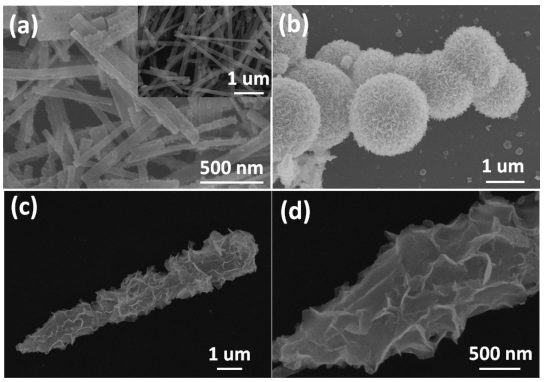

Figure 2. SEM images of (a) surface-coarsened TiO_2 nanobelts, TiO_2 nanobelts (top inset), (b) Bi_2MoO_6 nanosheets, and (c,d) Bi_2MoO_6 nanosheet/TiO_2 nanobelt (mole ratio 2:1) heterostructures.

nanosheet/TiO_2 nanobelt heterostructures with different mole ratios (1:1 and 4:1) are also obtained. The corresponding SEM images are presented in Figure S1. EDS (Figure S2) shows that Bi, Mo, and O elements are found in the Bi_2MoO_6 nanosheets, and Ti, Bi, Mo, and O elements are found in the Bi_2MoO_6 nanosheet/TiO_2 nanobelt heterostructures, and no other impurities are observed in the spectra.

The TEM image in Figure 3a shows that the TiO_2 nanobelt has a diameter of ~200 nm, which matches well with the above

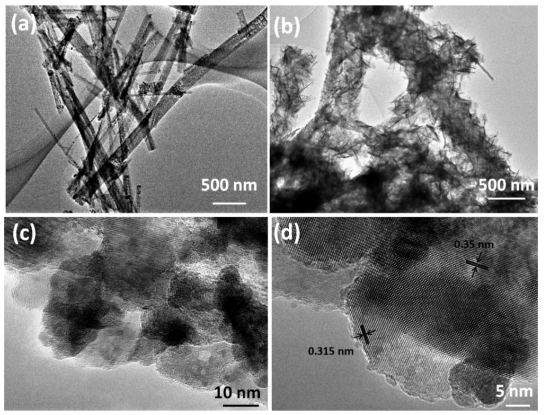

Figure 3. TEM images of (a) TiO_2 nanobelts and (b) Bi_2MoO_6 nanosheet/TiO_2 nanobelt (mole ratio 2:1) heterostructures; (c,d) high-magnification TEM images of Bi_2MoO_6 nanosheet/TiO_2 nanobelt (mole ratio 2:1) heterostructures.

SEM result (Figure 2a). After assembling Bi_2MoO_6 nanosheets on the surface of the TiO_2 nanobelts, the Bi_2MoO_6 nanosheet/TiO_2 nanobelt heterostructure still maintains a one-dimensional morphology. Bi_2MoO_6 nanosheets with a very thin layer could be observed on the surface of the TiO_2 nanobelts, which can be seen in Figure 3b. The high-resolution TEM images of Bi_2MoO_6 nanosheet/TiO_2 nanobelt heterostructures shown in Figure 3c and d reveal the interplanar spacing of 0.351 and 0.315 nm, which correspond to the (101) crystal planes of anatase TiO_2 and the (131) crystal planes of orthorhombic Bi_2MoO_6, respectively, indicating the formation of heterostructures.[27] The as-fabricated heterostructure has faster charge separation and more efficient carrier transfer compared with pure TiO_2 nanobelts or Bi_2MoO_6 nanosheets, and hence, the photocatalytic activities are improved.

3.2. Photocatalytic Performance. The photocatalytic properties of the Bi_2MoO_6 nanosheet/TiO_2 nanobelt heterostructures can be investigated by decomposition of aqueous MO solution under both UV and visible light irradiation (Figure 4). For comparison, Bi_2MoO_6 nanosheets, TiO_2

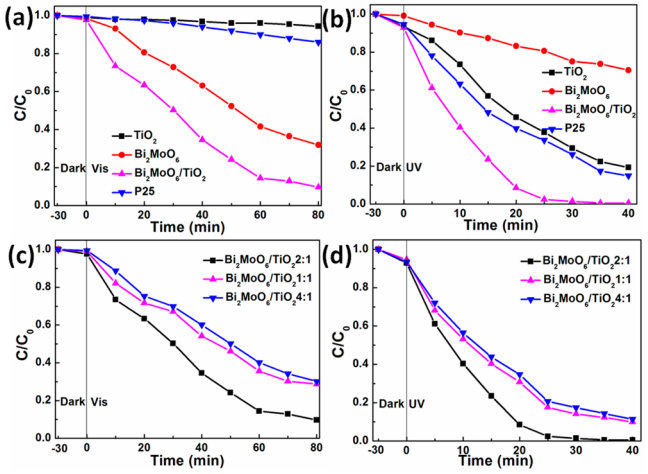

Figure 4. Photocatalytic decomposition of MO for P25, TiO_2 nanobelts, Bi_2MoO_6 nanosheets, and Bi_2MoO_6 nanosheet/TiO_2 nanobelt (mole ratio 2:1) heterostructures under (a) visible and (b) UV light irradiation. Photocatalytic decomposition of MO over Bi_2MoO_6 nanosheet/TiO_2 nanobelt heterostructures with different mole ratios under (c) visible and (d) UV light irradiation.

nanobelts, and P25 were used as photocatalytic references under the same experimental conditions. Before the photocatalysis, blank experiments were measured under the following conditions: (1) To achieve the adsorption equilibrium, the solution including MO and photocatalysts was stirred in the dark for 30 min and (2) without photocatalyst under UV and visible light irradiation. The above results illustrate that the samples by themselves exhibited no catalytic activity or absorption on MO in the dark (Figure 4). After 80 min in the absence of photocatalysts, the light irradiation hardly decomposed MO (Figure S3). It can be clearly seen that Bi_2MoO_6 nanosheet/TiO_2 nanobelt heterostructures display enhanced degradation efficiency under UV and visible light irradiation.

We see from Figure 4a that the TiO_2 nanobelts and P25 display a low photodegradation rate of MO under visible light irradiation because of their large band gap. The photodegradation rate of Bi_2MoO_6 nanosheets reaches 68.1% after 80 min of visible light irradiation; however, 90.4% of MO is photodegraded by the Bi_2MoO_6 nanosheet/TiO_2 nanobelt heterostructures, which is better than that of Bi_2MoO_6 nanosheets, TiO_2 nanobelts (5.7%), and P25 (14%). Under UV light irradiation (Figure 4b), almost 100% of the MO is photodegraded by Bi_2MoO_6 nanosheet/TiO_2 nanobelt heterostructures after 40 min, which is much better than that of P25, TiO_2 nanobelts, and Bi_2MoO_6 nanosheets. The degradation rates of MO for the pure TiO_2 nanobelts, Bi_2MoO_6 nanosheets, and P25 are 80.7%, 29.6%, and 85.1%, respectively, under 40 min UV light irradiation (Figure 4b). All of these measurements show that the Bi_2MoO_6 nanosheet/TiO_2 nanobelt heterostructures exhibit more prominent photocatalytic activity compared with the TiO_2 nanobelts or Bi_2MoO_6 nanosheets alone.

DOI: 10.1021/acscatal.5b00560
ACS Catal. 2015, 5, 4530−4536

The photocatalytic activities of the Bi_2MoO_6 nanosheet/TiO_2 nanobelt heterostructures with different Bi_2MoO_6/TiO_2 mole ratios are also studied (Figure 4c and d). As the mole ratio of Bi_2MoO_6/TiO_2 increases, the photocatalytic activities of Bi_2MoO_6 nanosheet/TiO_2 nanobelt heterostructures increase first, achieve a peak value at Bi_2MoO_6/TiO_2 = 2:1, and then decrease. The probable reasons are put forward as follows: Under visible light irradiation, at the low mole ratio (1:1), the photocatalytic property of the TiO_2 nanobelt is improved by being covered with a Bi_2MoO_6 nanosheet, which is a good visible photocatalyst and has a good light absorption in the visible region.[24] When the Bi_2MoO_6/TiO_2 mole ratio increases to 2:1, the photocatalytic property of the Bi_2MoO_6 nanosheet/TiO_2 nanobelt heterostructures can be enhanced with the increase in the Bi_2MoO_6 amount. After the maximum, the photocatalytic activity of Bi_2MoO_6 nanosheet/TiO_2 nanobelt heterostructure decreases with the increase in the Bi_2MoO_6/TiO_2 mole ratio (4:1). This could be caused by excessive Bi_2MoO_6 that covers the active sites of TiO_2 nanobelts (Figure S1c and d), which hinders the electron transfer on the interface of the Bi_2MoO_6 nanosheet/TiO_2 nanobelt heterostructures and, thus, in turn inhibits the photoactivity. For UV irradiation, when the mole ratio is 1:1, the photocatalytic property of the Bi_2MoO_6 nanosheet/TiO_2 nanobelt heterostructure is a little better than that of TiO_2 nanobelts. When the mole ratio of Bi_2MoO_6/TiO_2 is 2:1, the uniform layer of Bi_2MoO_6 nanosheets covering the TiO_2 nanobelts forming the heterostructures induce the best UV photocatalytic property. The heterostructures can promote the separation of photogenerated carriers; thus, the photocatalytic properties are improved. After the mole ratio of Bi_2MoO_6/TiO_2 increases to 4:1, the photocatalytic property drops with an increase in the Bi_2MoO_6/TiO_2 mole ratio because aggregated Bi_2MoO_6 nanosheets on the surface of TiO_2 nanobelts have a smaller specific surface area (Figure S1c and d).

To investigate the photocatalytic stability of the photocatalysts, the photodegradation of MO with the same photocatalysts was measured for four cycles. After each cycle, the photocatalyst was filtered and dried thoroughly, and then the fresh MO solution was added. As is shown in Figure 5, after

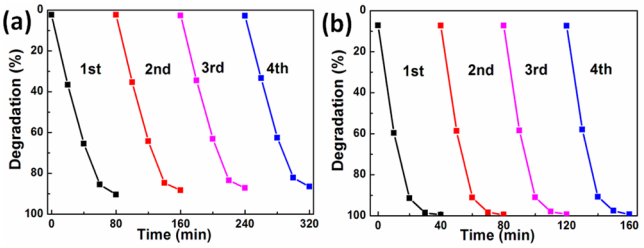

Figure 5. Irradiation-time dependence of photocatalytic decomposition of MO solution for Bi_2MoO_6 nanosheet/TiO_2 nanobelt heterostructures after four cycles under (a) visible and (b) UV light irradiation.

four cycles, the Bi_2MoO_6 nanosheet/TiO_2 nanobelt (mole ratio 2:1) heterostructures still maintain good photocatalytic stability under UV and visible light irradiation (Figure 5).

The FTIR spectra (Figure 6) were taken on the Bi_2MoO_6 nanosheet/TiO_2 nanobelt heterostructures in the MO solution in the dark for 30 min to verify whether MO is absorbed by the heterostructures. The FTIR spectra of MO (Figure 6a) show peaks at 1036.7, 1119.1, and 2924.06 cm^{-1} corresponding to

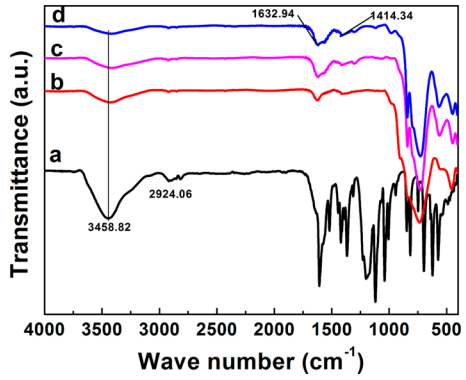

Figure 6. FTIR spectra of (a) methyl orange (MO), (b) Bi_2MoO_6 nanosheet/TiO_2 nanobelt heterostructures, (c) Bi_2MoO_6 nanosheet/TiO_2 nanobelt (mole ratio 2:1) heterostructures in the MO solution in the dark for 30 min, and (d) Bi_2MoO_6 nanosheet/TiO_2 nanobelt (mole ratio 2:1) heterostructures in the MO solution under visible light irradiation for 30 min.

ring vibrations, −C−N fingerprints of dye, and $-CH_3$ stretching vibrations, respectively. For the FTIR spectra of pure Bi_2MoO_6 nanosheet/TiO_2 nanobelt heterostructures (Figure 6b), the peaks at 1414.34, 1632.94, and 3458.82 cm^{-1} correspond to the banding of −OH groups.[28,29] After the heterostructure in MO solutions is kept in the dark and under visible light for 30 min (Figure 6c and d), only the peaks of the Bi_2MoO_6 nanosheet/TiO_2 nanobelt heterostructures can be observed; none match MO. The total organic carbon (Figure S4) of MO solutions with heterostructure as the photocatalyst after visible light irradiation indicates that MO had been well photodegraded.

To further understand the improvement of photocatalytic activity of Bi_2MoO_6 nanosheet/TiO_2 nanobelt heterostructures, PEC performances of TiO_2 nanobelts, Bi_2MoO_6 nanosheets, and Bi_2MoO_6 nanosheet/TiO_2 nanobelt heterostructures as photoanodes were investigated. Figure 7 presents the photo-

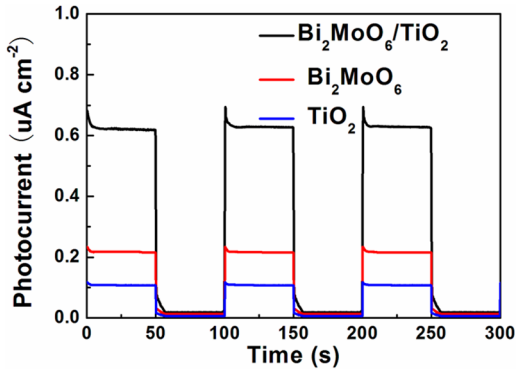

Figure 7. Photocurrent response of the photoanodes with TiO_2 nanobelts, Bi_2MoO_6 nanosheets, and Bi_2MoO_6 nanosheet/TiO_2 nanobelt (mole ratio 2:1) heterostructures in the dark and under solar simulator irradiation in 0.1 M Na_2SO_4 solutions.

current response of samples at a 0.8 V bias vs SCE under solar simulator irradiation. It can be found that the Bi_2MoO_6 nanosheet/TiO_2 nanobelt heterostructures exhibit enhanced photocurrents (70 uA/cm^2) compared with Bi_2MoO_6 nanosheets (24 uA/cm^2) and TiO_2 nanobelts (0.9 uA/cm^2). The higher photocurrent density of Bi_2MoO_6 nanosheet/TiO_2 nanobelt heterostructure photoelectrodes indicates an en-

DOI: 10.1021/acscatal.5b00560
ACS Catal. 2015, 5, 4530−4536

hanced light absorption and improved separation of photogenerated carriers.

The photocatalytic activity of the Bi_2MoO_6 nanosheet/TiO_2 nanobelt heterostructures can also be tested by measuring the photocatalytic oxygen production activities (Figure 8). The

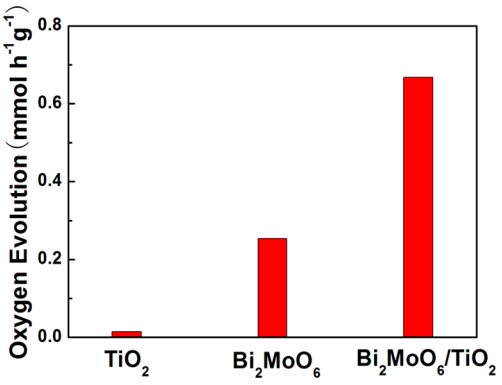

Figure 8. Photocatalytic oxygen production activities of TiO_2 nanobelts, Bi_2MoO_6 nanosheets and Bi_2MoO_6 nanosheet/TiO_2 nanobelt (mole ratio 2:1) heterostructures under a Xe arc lamp illumination.

TiO_2 nanobelts present poor photocatalytic oxygen production activity (0.006 mmol h^{-1} g^{-1}) because they can use only the UV light; however, the Bi_2MoO_6 nanosheet/TiO_2 nanobelt (mole ratio 2:1) heterostructures exhibit the highest oxygen evolution rate of 0.668 mmol h^{-1} g^{-1}, which is better than that of the Bi_2MoO_6 nanosheets (0.254 mmol h^{-1} g^{-1}) and Bi_2MoO_6 nanosheet/TiO_2 nanobelt heterostructures at other mole ratios (Figure S5). The obvious photocatalytic oxygen production activities can be attributed to the improved visible light absorption of Bi_2MoO_6 nanosheets.[24] Importantly, the positive effect from the heterostructure makes the photocatalytic oxygen production activity of Bi_2MoO_6 nanosheet/TiO_2 nanobelt heterostructures better than that of the Bi_2MoO_6 nanosheets. Therefore, in the Bi_2MoO_6 nanosheet/TiO_2 nanobelt heterostructures, Bi_2MoO_6 nanosheets are capable visible light harvesters, and the heterostructures can provide efficient charge separation; thus, the photocatalytic activity of the oxygen production is improved.

Figure 9 shows UV−vis DRS of TiO_2 nanobelts, Bi_2MoO_6 nanosheets, and Bi_2MoO_6 nanosheet/TiO_2 nanobelt heterostructures. The absorption of the TiO_2 nanobelts is located in

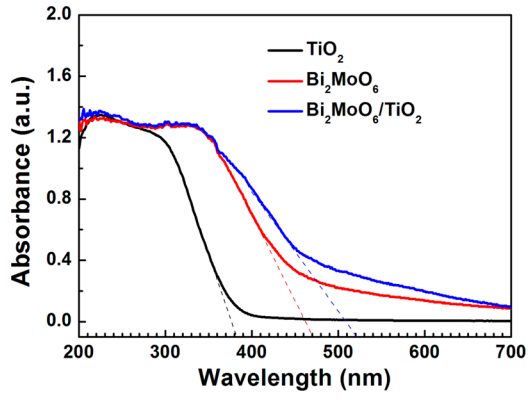

Figure 9. UV−vis DRS of TiO_2 nanobelts, Bi_2MoO_6 nanosheets, and Bi_2MoO_6 nanosheet/TiO_2 nanobelt (mole ratio 2:1) heterostructures.

the UV region. The absorption cutoff edge is ~393 nm (curve a), which agrees well with the bandgap energy (E_g) of anatase;[17] however, the absorption edges of the Bi_2MoO_6 nanosheets extend the absorption edge to 470 nm (curve b). Upon the growth of thin Bi_2MoO_6 nanosheets on the surface of TiO_2 nanobelts, the visible light absorption ability of Bi_2MoO_6 nanosheet/TiO_2 nanobelt heterostructures is greatly improved (curve c) in comparison with TiO_2 nanobelts, and the absorption edges are located at ~521 nm. Compared with the Bi_2MoO_6 nanosheets with its absorption edge at 470 nm, the large red shift of absorption of the heterostructure arises from the surface morphological change from a sphere to a 3D porous structure. This larger absorption would result in the improvement of the photocatalytic property of Bi_2MoO_6 nanosheet/TiO_2 nanobelt heterostructures. The absorption edge of TiO_2 nanobelts, Bi_2MoO_6 nanosheets, and Bi_2MoO_6 nanosheet/TiO_2 nanobelt heterostructures is 393, 470, and 521 nm, respectively (Figure 9); therefore, their E_g is 3.15, 2.64, and 2.38 eV, respectively.

Photoluminescence (PL) spectra can study the separation efficiency of the photogenerated carriers. Figure 10 shows the

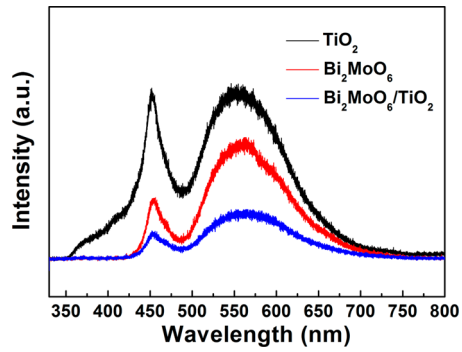

Figure 10. Photoluminescence (PL) spectra of TiO_2 nanobelts, Bi_2MoO_6 nanosheets and Bi_2MoO_6 nanosheet/TiO_2 nanobelt (mole ratio 2:1) heterostructures, λ_{ex} = 325 nm.

PL spectra of the TiO_2 nanobelts, Bi_2MoO_6 nanosheets, and Bi_2MoO_6 nanosheet/TiO_2 nanobelt heterostructures. The TiO_2 nanobelts show two distinct emission peaks at 450 and 525 nm, which belong to the emission of the band gap transition.[17] The Bi_2MoO_6 nanosheets also exhibit two strong emission peaks, which might be due to the intrinsic luminescence properties of Bi_2MoO_6.[30] The Bi_2MoO_6 nanosheet/TiO_2 nanobelt heterostructures show a weaker emission peak than that of TiO_2 nanobelts and Bi_2MoO_6 nanosheets, which indicates that the heterostructure between TiO_2 and Bi_2MoO_6 can effectively diminish the recombination of photogenerated carriers; hence, the photocatalytic activity is enhanced.

3.3. Mechanisms of Improved Photocatatic Properties. The improved photocatalytic property of the Bi_2MoO_6 nanosheet/TiO_2 nanobelt heterostructures under UV and visible light irradiation may be attributed to the following factors:

First, according to DRS analysis (Figure 4), Bi_2MoO_6 nanosheet/TiO_2 nanobelt heterostructures have a narrow band gap and exhibit enhanced UV and visible light absorption. The Bi_2MoO_6 nanosheet/TiO_2 nanobelt heterostructures can absorb more UV and visible light than Bi_2MoO_6 nanosheets, and thus, the photocatalytic activities are enhanced.

Second, the Bi_2MoO_6 nanosheet/TiO_2 nanobelt heterostructures have a larger specific surface area. The Bi_2MoO_6

DOI: 10.1021/acscatal.5b00560
ACS Catal. 2015, 5, 4530−4536

nanosheet/TiO_2 nanobelt heterostructures have a higher BET surface area (42.91 $m^2 g^{-1}$) than that of TiO_2 nanobelts (19.01 $m^2 g^{-1}$) and Bi_2MoO_6 nanosheets (26.377 $m^2 g^{-1}$). The high surface area of this 3D heterostructure allows not only more surfaces to be reached by the incident light but also more sites on the surface for the adsorption and photodegradation of MO, which results in enhanced photocatalytic performance. It is also well-known that materials with a larger specific surface area could adsorb more oxygen on their surface.[31] The Bi_2MoO_6 nanosheet/TiO_2 nanobelt heterostructures have larger specific surface areas, and therefore, they could absorb more oxygen (oxygen could react with electrons in the photocatalytic process), which also results in a higher efficiency in the photocatalysis.

In addition, the heterostructure formed between Bi_2MoO_6 and TiO_2 can effectively suppress the recombination of photoelectrons and holes. This is another reason to explain the excellent photocatalytic performance of Bi_2MoO_6 nanosheet/TiO_2 nanobelt heterostructures. In this work, we successfully realize a close contact of Bi_2MoO_6 nanosheets with TiO_2 nanobelts in the Bi_2MoO_6 nanosheet/TiO_2 nanobelt heterostructures. Such close contacts can effectively suppress the recombination between photoelectrons and holes, which results in longer lifetimes for both of them. These well-separated electrons and holes could further take part effectively in the overall photocatalysis. Having fewer existing barriers between Bi_2MoO_6 and TiO_2 also promotes the migration of photogenerated carriers.

Finally, a 3D porous structure can enhance the photon utilization efficiency and improve the contact between pollutants and photocatalysts. Bi_2MoO_6 nanosheets covering the surface of TiO_2 nanobelts form the 3D porous structure. A suitable conformation of pores allows a great number of the photons to penetrate deep inside the photocatalyst, and many photons remain trapped within the porous structure until being completely absorbed. This might explain why the 3D porous Bi_2MoO_6 nanosheet/TiO_2 nanobelt heterostructures present higher photocatalytic properties than that of the Bi_2MoO_6 nanosheets and TiO_2 nanobelts.

On the basis of the above discussion, it is obvious that the generation and separation process of electron−hole can be efficiently promoted by the interaction between Bi_2MoO_6 and TiO_2 under UV and visible light irradiation. An electron−hole separation mechanism is shown in Scheme 1. The positions of conduction and valence band can be calculated by the following equation,[17]

$$E_{CB} = X - E_e - 0.5E_g \quad (1)$$

Scheme 1. Schematic Diagram of Electron-Hole Separation Mechanism upon UV−vis Excitation for Bi_2MoO_6 Nanosheet/TiO_2 Nanobelt Heterostructures

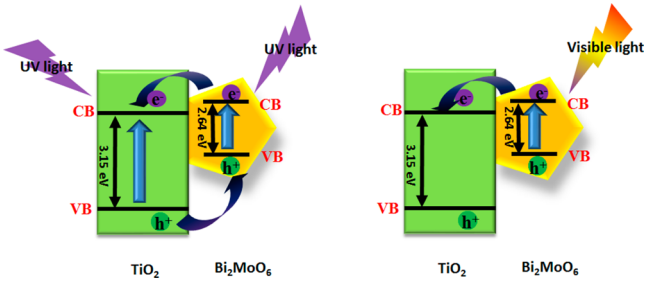

where E_{CB} is the CB edge potential. The X values for TiO_2 and Bi_2MoO_6 are about 5.81 and 5.54 eV, respectively.[17,32] The E_e value is ~4.5 eV. The E_g values of TiO_2 and Bi_2MoO_6 are 3.15 and 2.64 eV, respectively. The E_{CB} values are calculated at about −0.27 and −0.28 eV. Correspondingly, the VB edge potentials (E_{VB}) are estimated to be about 2.88 and 2.36 eV, respectively.

As shown in Scheme 1, under UV light irradiation, both TiO_2 and Bi_2MoO_6 can be excited: the photogenerated electrons in their CB and holes in the VB generate. Because the E_{VB} of TiO_2 (2.88 eV) is more positive than that of Bi_2MoO_6 (2.36 eV), holes in the VB of TiO_2 can migrate to the VB of Bi_2MoO_6 by the interface. Similarly, the E_{CB} of Bi_2MoO_6 (−0.28 eV) is lower than that of TiO_2 (−0.27 eV): the electrons in the CB of Bi_2MoO_6 can transfer to the CB of TiO_2, thus hindering photoinduced electron−hole recombination in TiO_2 and Bi_2MoO_6, which results in the enhancement of photocatalytic property under UV light irradiation. When exposed to visible light, only the electrons in the VB of Bi_2MoO_6 can be excited. The electrons in the CB of TiO_2 can migrate to the CB of Bi_2MoO_6, which leads to the separation of carriers.

4. CONCLUSIONS

In summary, the novel 3D Bi_2MoO_6 nanosheet/TiO_2 nanobelt heterostructures are prepared via a simple and efficient hydrothermal method. A dense layer of Bi_2MoO_6 ultrathin nanosheets are loaded onto the surface of TiO_2 nanobelts. Importantly, the heterostructure exhibits excellent photocatalytic decomposition of organic dyes properties and water-splitting for oxygen production under UV and visible light. Furthermore, the heterostructure also shows an enhanced photoelectochemistry performance and good photocatalytic stability. The enhanced performance can be ascribed to its 3D flake-like porous structure, large specific surface area, large matched energy band of heterostructure, improved charge transfer efficiency,. and suppressed photoelectron−hole recombination. We believe that the development of the high photocatalytic activities of 3D heterostructures will provide a promising platform for high-performance photocatalytic applications.

■ ASSOCIATED CONTENT

Supporting Information

The Supporting Information is available free of charge on the ACS Publications website at DOI: 10.1021/acscatal.5b00560.

SEM images of Bi_2MoO_6 nanosheet/TiO_2 nanobelt (mole ratio 1:1) heterostructures and Bi_2MoO_6 nanosheet/TiO_2 nanobelt (mole ratio 4:1) heterostructures, EDS of Bi_2MoO_6 nanosheet and Bi_2MoO_6 nanosheet/TiO_2 nanobelt (mole ratio 2:1) heterostructures, photocatalytic degradation of MO for comparison tests (PDF)

■ AUTHOR INFORMATION

Corresponding Authors

*Phone: +86-532-86057929. Fax: +86-532-86057929. E-mail: cuihongzhi1965@163.com.

*Phone: +86-531- 88362807. Fax: +86-531- 88362807. E-mail: hongliu@sdu.edu.cn.

Notes

The authors declare no competing financial interest.

DOI: 10.1021/acscatal.5b00560
ACS Catal. 2015, 5, 4530−4536

■ ACKNOWLEDGMENTS

The authors are thankful for fundings from the National Natural Science Foundation of China (No. 51372142 and 51272141), Taishan Scholars Project of Shandong Province (No. TS20110828), National High Technology Research and Development Program of China (863 Program, No. 2015AA034404), Innovation Research Group (IRG: 51321091), and the "100 Talents Program" of the Chinese Academy of Sciences.

■ REFERENCES

(1) Wang, L.; Sasaki, T. *Chem. Rev.* **2014**, *114*, 9455−9486.
(2) Li, Z.; Wang, F.; Kvit, A.; Wang, X. *J. Phys. Chem. C* **2015**, *119*, 4397−4405.
(3) Xiao, F. X.; Hung, S. F.; Miao, J.; Wang, H. Y.; Yang, H.; Liu, B. *Small* **2015**, *11*, 554−567.
(4) Tian, J.; Zhao, Z.; Kumar, A.; Boughton, R. I.; Liu, H. *Chem. Soc. Rev.* **2014**, *43*, 6920−6937.
(5) Xu, H.; Chen, R.; Sun, Q.; Lai, W.; Su, Q.; Huang, W.; Liu, X. *Chem. Soc. Rev.* **2014**, *43*, 3259−3302.
(6) Chen, J.; Yang, H. B.; Miao, J.; Wang, H. Y.; Liu, B. *J. Am. Chem. Soc.* **2014**, *136*, 15310−15318.
(7) Liu, B.; Khare, A.; Aydil, E. S. *ACS Appl. Mater. Interfaces* **2011**, *3*, 4444−4450.
(8) Zhang, H.; Liu, X.; Li, Y.; Sun, Q.; Wang, Y.; Wood, B. J.; Zhao, H.; Liu, P.; Yang, D. *J. Mater. Chem.* **2012**, *22*, 2465−2472.
(9) Zhou, R.; Zhang, Q.; Uchaker, E.; Lan, J.; Yin, M.; Cao, G. *J. Mater. Chem. A* **2014**, *2*, 2517−2525.
(10) Yang, L.; McCue, C.; Zhang, Q.; Uchaker, E.; Mai, Y.; Cao, G. *Nanoscale* **2015**, *7*, 3173−3180.
(11) Liu, B.; Liu, L. M.; Lang, X. F.; Wang, H. Y.; Lou, X. W. D.; Aydil, E. S. *Energy Environ. Sci.* **2014**, *7*, 2592−2597.
(12) Yang, H. B.; Miao, J.; Hung, S. F.; Huo, F.; Chen, H. M.; Liu, B. *ACS Nano* **2014**, *8*, 10403−10413.
(13) Sakthivel, S.; Kisch, H. *Angew. Chem., Int. Ed.* **2003**, *42*, 4908−4911.
(14) Naldoni, A.; Allieta, M.; Santangelo, S.; Marelli, M.; Fabbri, F.; Cappelli, S.; Bianchi, C. L.; Psaro, R.; Dal Santo, V. *J. Am. Chem. Soc.* **2012**, *134*, 7600−7603.
(15) Zhou, W.; Liu, H.; Wang, J.; Liu, D.; Du, G.; Cui, J. *ACS Appl. Mater. Interfaces* **2010**, *2*, 2385−2392.
(16) Lin, J.; Shen, J.; Wang, R.; Cui, J.; Zhou, W.; Hu, P.; Liu, D.; Liu, H.; Wang, J.; Boughton, R. I.; Yue, Y. *J. Mater. Chem.* **2011**, *21*, 5106−5113.
(17) Tian, J.; Sang, Y.; Zhao, Z.; Zhou, W.; Wang, D.; Kang, X.; Liu, H.; Wang, J.; Chen, S.; Cai, H.; Huang, H. *Small* **2013**, *9*, 3864−3872.
(18) Tian, J.; Sang, Y.; Yu, G.; Jiang, H.; Mu, X.; Liu, H. *Adv. Mater.* **2013**, *25*, 5075−5080.
(19) Wang, X.; Li, Z.; Shi, J.; Yu, Y. *Chem. Rev.* **2014**, *114*, 9346−9384.
(20) Tian, G.; Chen, Y.; Zhai, R.; Zhou, J.; Zhou, W.; Wang, R.; Pan, K.; Tian, C.; Fu, H. *J. Mater. Chem. A* **2013**, *1*, 6961−6968.
(21) Wei, W.; Dai, Y.; Huang, B. *J. Phys. Chem. C* **2009**, *113*, 5658−5663.
(22) Zhang, M.; Shao, C.; Mu, J.; Zhang, Z.; Guo, Z.; Zhang, P.; Liu, Y. *CrystEngComm* **2012**, *14*, 605−612.
(23) Shimodaira, Y.; Kato, H.; Kobayashi, H.; Kudo, A. *J. Phys. Chem. B* **2006**, *110*, 17790−17797.
(24) Bi, J.; Wu, L.; Li, J.; Li, Z.; Wang, X.; Fu, X. *Acta Mater.* **2007**, *55*, 4699−4705.
(25) Guo, C.; Xu, J.; Wang, S.; Li, L.; Zhang, Y.; Li, X. *CrystEngComm* **2012**, *14*, 3602−3608.
(26) Tian, J.; Leng, Y.; Zhao, Z.; Xia, Y.; Sang, Y.; Hao, P.; Liu, H.; Zhan, J.; Li, M. *Nano Energy* **2015**, *11*, 419−427.
(27) Tian, G.; Chen, Y.; Zhai, R.; Zhou, J.; Zhou, W.; Wang, R.; Pan, K.; Tian, C.; Fu, H. *J. Mater. Chem. A* **2013**, *1*, 6961−6968.
(28) Fang, Q.; Chen, B. *Carbon* **2012**, *50*, 2209−2219.
(29) Tursiloadi, S.; Imai, H.; Hirashima, H. *J. Non-Cryst. Solids* **2004**, *350*, 271−276.
(30) Tian, G.; Chen, Y.; Zhou, J.; Tian, C.; Li, R.; Wang, C.; Fu, H. *CrystEngComm* **2014**, *16*, 842−849.
(31) Lu, B.; Li, X.; Wang, T.; Xie, E.; Xu, Z. *J. Mater. Chem. A* **2013**, *1*, 3900−3906.
(32) Long, M.; Cai, W.; Kisch, H. *Chem. Phys. Lett.* **2008**, *461*, 102−105.

DOI: 10.1021/acscatal.5b00560
ACS Catal. 2015, 5, 4530−4536